ELSEVIER

Contents lists available at ScienceDirect

Chemical Engineering Journal

journal homepage: www.elsevier.com/locate/cej





A self-assembled nanoporous polyelectrolytic interlayer for highly stable zinc metal anodes

Siyu Tian ^a, Long Zhou ^a, Wei He ^b, Yafen Tian ^c, Yue Zhou ^a, Shiwen Wu ^a, Ruda Jian ^a, Kenneth J. Balkus ^c, Tengfei Luo ^d, Guoping Xiong ^{a,*}

- a Department of Mechanical Engineering, The University of Texas at Dallas, 800 W Campbell Rd, Richardson, TX 75080, United States
- b Department of Electrical Engineering and Computer Science, South Dakota State University, 1451 Stadium Rd, Brookings, SD 57007, United States
- Eppartment of Chemistry & Biochemistry, The University of Texas at Dallas, 800 W Campbell Rd, Richardson, TX 75080, United States
- d Aerospace and Mechanical Engineering, University of Notre Dame, Notre Dame, IN 46556, United States

ARTICLE INFO

Keywords: Polyelectrolytes Nanoporous Dendrite growth Hydrogen evolution Zinc metal anodes Zinc-ion batteries

ABSTRACT

Aqueous zinc-ion batteries (AZIBs) based on Zn metal anodes are promising candidates for next-generation energy storage due to their high performance, environmental friendliness, low cost, and high abundance. However, the excessive dendrite growth and continuous hydrogen evolution of Zn metal anodes in aqueous electrolytes severely deteriorate the electrochemical performance of AZIBs. Here, a highly stable Zn metal anode is designed by reconstructing its surface with a self-assembled nanoporous polyelectrolytic interlayer. This unique protective layer consisting of polyacrylic acid-zinc (PAAZn) nanospheres is highly hydrophilic and can act as a physical barrier to reduce the contact between Zn metal and water molecules, thus suppressing hydrogen evolution and Zn corrosion. Meanwhile, the unique nanostructures and chemical compositions of the PAAZn interlayer ensure fast Zn plating/stripping kinetics and facilitate the homogeneous growth of Zn deposits by redistributing Zn ion flux and local electric field at Zn/electrolyte interfaces. Therefore, symmetric cells based on the PAAZn-modified Zn metal anode (PAAZn@Zn) exhibited a significantly prolonged cycle life of 2,850 h and low voltage hysteresis. This work reports a uniquely designed nanoporous polyelectrolytic interlayer for highly reversible Zn metal anodes and provides a new strategy to enhance the electrochemical performance of AZIBs.

1. Introduction

Rechargeable aqueous batteries are promising candidates for safe, low-cost, and eco-friendly energy storage in a wide range of applications from wearable devices to grid-scale applications [1,2]. Among them, aqueous zinc-ion batteries (AZIBs) based on Zn metal anodes have become competitive candidates because of their high theoretical capacity (820 mAh/g), high elemental availability, low toxicity, and relatively good stability in aqueous electrolytes [3,4]. However, the widespread usage of AZIBs remains a significant challenge arising from the unfavorable interfacial chemistry of Zn metal anodes, including severe dendrite growth, fast corrosion, and inevitable parasitic reactions (e.g., hydrogen evolution reaction – HER) [5,6]. Particularly, the irregular morphology and preferential growth of Zn deposits and the uneven ion diffusion within cells result in the continuous, vertical growth of Zn dendrites during long-term charge/discharge processes [7,8]. The uncontrollable dendrite growth will severely deteriorate the

electrochemical performance and induce the internal short circuit in batteries. Therefore, regulating dendrite growth at the Zn/electrolyte interface is essential to enable highly reversible Zn metal anodes and realize the widespread use of AZIBs.

In recent years, considerable efforts have been made to improve the reversibility of Zn metal anodes and the electrochemical performance of AZIBs. For instance, incorporating various additives into bulk electrolytes, such as 2 M ZnSO₄, has been shown to effectively improve the reversibility of Zn metal anodes [9–11]. Other techniques, including functionalizing the separators, reconstructing the Zn surface morphologies, and controlling the crystallographic characteristics of Zn metal, can also suppress the dendrite growth and extend the cycle life of AZIBs [12–15]. Although these methods could improve the reversibility of Zn metal anodes, complicated fabrication processes and high cost severely hinder their practical applications. In this regard, low-cost and scalable strategies by constructing artificial interlayers between Zn metal and electrolyte have shown great potential to stabilize Zn metal anodes in

E-mail address: guoping.xiong@utdallas.edu (G. Xiong).

^{*} Corresponding author.

aqueous environments. To date, a wide range of metallic, organic, and inorganic materials such as liquid alloy [16], Ag [17], Cu [18], Au [19], carbon-based materials [20,21], gelatin [22], poly zwitterionic ionic liquid [5], polymeric materials [23,24], Al₂O₃ [25], TiO₂ [26-28], CaCO₃ [29], SiO₂ [30] and ZrO₂ [31,32] have been reported as artificial interlayers. Among them, polymeric interlayers containing abundant hydrophilic and zincophilic functional groups are promising candidates due to their ability to regulate dendrite growth and stabilize Zn metal anodes by redistributing Zn ion flux, suppressing side reactions, and homogenizing charge distributions at the artificial interfaces [33]. However, fundamental limitations still exist in conventional polymeric materials since the ion transport is strongly restricted by the slow segmental relaxation of polymer chains, leading to low capacities and poor cycle life in batteries [34,35]. Therefore, designing new polymeric interlayers that facilitate ion transport through the artificial interfaces remains an open challenge in the pursuit of highly stable Zn metal anodes.

Here, we report a self-assembled nanoporous polyelectrolytic interlayer to regulate dendrite growth and suppress hydrogen evolution to achieve highly reversible Zn metal anodes. The electrochemically inert polyacrylic acid-zinc (PAAZn) nanospheres with abundant zincophilic carboxyl groups and electrostatically bonded Zn ions can effectively promote homogeneous Zn deposition, as confirmed by scanning electron microscopy (SEM). Moreover, the uniquely designed nanoporous interlayer is conducive to protect Zn metal from corrosions and undesirable parasitic reactions in aqueous electrolytes, while ensuring rapid Zn-ion diffusions and fast charge transfer kinetics at the nanoporous PAAZn-modified interfaces. Due to these advantages, the symmetric cells based on PAAZn-modified Zn metal anode (PAAZn@Zn) exhibited low voltage hysteresis and long cycle life at various current densities (e.g., 2,850 h at 1 mA/cm², 800 h at 5 mA/cm²). When paired with sodium-doped vanadium oxide (NVO) cathodes, assembled PAAZn@Zn||NVO

full cells displayed significantly increased stability compared with bare Zn||NVO cells, rendering the uniquely designed PAAZn@Zn anodes a promising candidate for high-performance AZIBs.

2. Results and discussions

The PAAZn@Zn anodes were prepared via a facile solution-based process by etching bare Zn in aqueous polyacrylic acid (PAA) solutions, resembling the synthesis of PAA-metal (e.g., Li, Zn, Ca) complexes reported in prior work [36-38]. During the etching process (Fig. S1), gas bubbles were produced continuously via chemical reactions, and PAAZn complex was subsequently formed on the Zn surface. Fig. 1a schematically shows the overall chemical reaction between PAA and Zn metal in aqueous environments. This overall reaction includes three steps, as illustrated in Fig. S2. In the first step, PAA molecules become negatively charged (PAA⁻) accompanied by the release of protons (H⁺) because of the ionization of carboxyl groups [39]. Then, these protons react with Zn metal to form Zn²⁺ in aqueous environments and result in the generation of bubbles, which could be hydrogen (step 2). Finally, the localized Zn ions are electrostatically bonded with negatively charged PAA⁻ chains to form a complex of PAAZn (step 3), similar to the complexation between PAA and metal ions such as Li⁺, Zn²⁺, and Ca²⁺ reported in previous studies [36-38]. Consequently, a layer of PAAZn nanospheres could be self-assembled on the surface of Zn via electrostatic interactions, as schematically illustrated in Fig. S3. In contrast to bare Zn with a typical metallic grey surface, the etched Zn (PAAZn@Zn) exhibited a matte-like surface (Fig. 1b) in the presence of the selfassembled interlayer.

Fig. 1c-f shows the SEM images of bare Zn and PAAZn@Zn. The surface of bare Zn displayed an irregular morphology in the presence of many trenches (Fig. 1c and Fig. S4a) and defects (Fig. 1d). In contrast, PAAZn@Zn exhibited a distinctly different morphology (Fig. 1e-f and

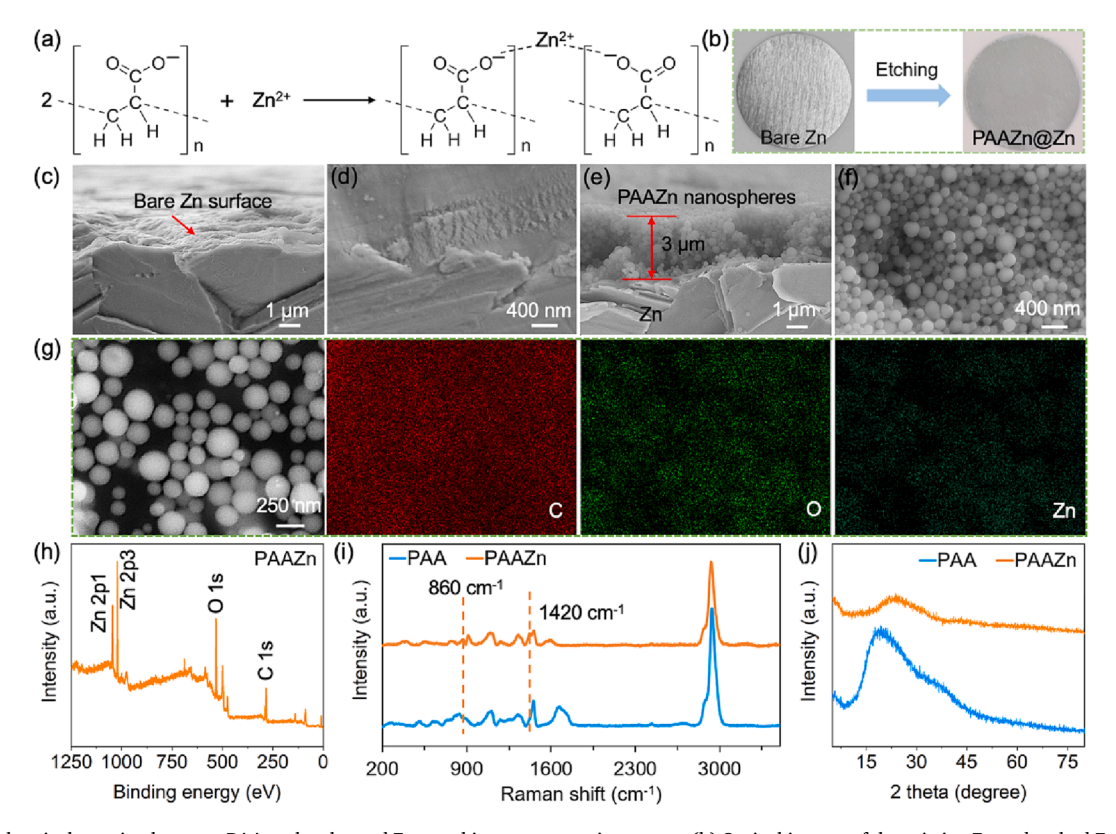


Fig. 1. (a) The chemical reaction between PAA molecules and Zn metal in aqueous environments. (b) Optical images of the pristine Zn and etched Zn disks (14 mm in diameter). SEM images showing the morphology of the (c) cross section and (d) top surface of bare Zn, (e) cross section and (f) top surface of PAAZn@Zn. (g) EDAX mapping of the self-assembled PAAZn nanospheres exfoliated on a carbon tape showing the elemental distributions of C, O, and Zn. Characterization of pure PAA and PAAZn nanospheres: (h) XPS, (i) Raman spectroscopy, and (j) XRD.

Fig. S4b), and the entire surface of PAAZn@Zn was covered by a thin (e. g., 3 μm) layer of nanospheres. As the etching time increased from 6 to 24 h (Fig. S5), the thickness of the interfacial layer increased from approximately 318 nm to 3 μm , and the nanospheres were packed more densely. However, as shown in Fig. S6, the Zn substrates before and after being etched by PAA solutions for 24 h exhibited a similar flat surface, suggesting that the etching process had no significant effect on the flatness of the Zn substrates. In addition, because of the self-assembled nanoporous interlayer, PAAZn@Zn exhibited a water contact angle of 36.0°, significantly smaller than that (77.8°) of bare Zn (Fig. S7), signifying the excellent hydrophilicity that could facilitate electrolyte wetting on the chemically modified Zn metal surface.

To analyze the chemical structures of these polyelectrolytic nanospheres, energy dispersive X-ray analysis (EDAX), X-ray photoelectron spectroscopy (XPS), Raman spectroscopy, X-ray diffraction (XRD), and Fourier transform inferred (FTIR) tests were conducted. Fig. 1g shows the SEM image and the corresponding elemental distributions of PAAZn nanospheres. The EDAX mapping and spectrum (Fig. S8) of the PAAZn nanospheres revealed that these nanospheres contained three elemental compositions: carbon (C), oxygen (O), and zinc (Zn). The O and Zn

elements were well-confined within the region of nanospheres. Fig. 1h shows the XPS spectrum of PAAZn nanospheres. The characteristic peaks of C, O and Zn were clearly observed in the spectrum. Particularly, the two peaks located at 1,022 (Zn 2p3) and 1,045 (Zn 2p1) eV can be attributed to ionically bonded $\rm Zn^{2+}$ [40], confirming the existence of $\rm Zn^{2+}$ in the nanospheres. In addition, semi-quantitative analysis of the XPS spectrum indicated that the atomic ratio of C:O:Zn in the PAAZn nanospheres was 51.2:34.3:14.5, implying that the –COOH groups in PAA molecules were only partially substituted by $\rm Zn^{2+}$ during etching. Note that the C:O atomic ratio in PAAZn nanospheres was 1.49, close to that (1.50) of pure PAA according to its chemical formula (CH₂-CH-COOH)_n.

Fig. 1i presents the Raman spectra of pure PAA and PAAZn nanospheres. For pure PAA, several characteristic peaks were observed, including C–CH₂ vibration at 1,114 cm $^{-1}$, C–H vibration at 2,934 cm $^{-1}$, –COOH vibration at 861 cm $^{-1}$, –CH₂– vibration at 1,454 cm $^{-1}$ and C=O stretching vibration at 1,685 cm $^{-1}$ [41–43]. Upon complexation with Zn²⁺, the peaks associated with C–CH₂ and C–H vibrations remained largely unchanged, while the peaks assigned to –CH₂–, –COOH, and C=O vibrations shifted due to the strong electrostatic interactions

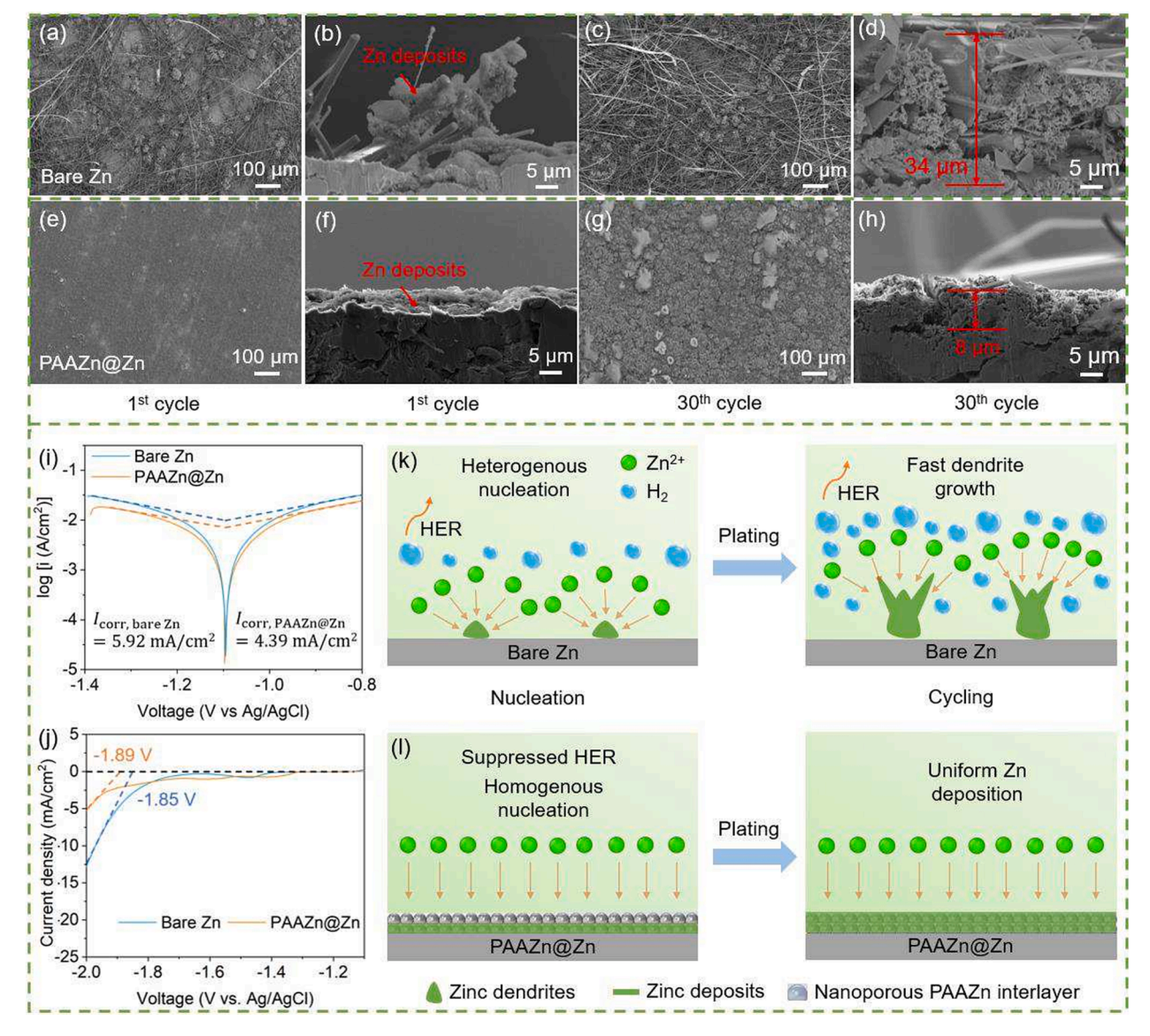


Fig. 2. SEM images of cycled bare Zn anodes showing the morphologies of (a), (c) top surface and (b), (d) cross section. SEM images of cycled PAAZn@Zn anodes showing the morphologies of: (e), (g) top surface and (f), (h) cross section. (i) Tafel curves and (j) LSV curves of bare Zn and PAAZn@Zn electrodes. Schematic illustration of Zn plating on the surface of (k) bare Zn and (l) PAAZn@Zn.

between $\rm Zn^{2+}$ and $\rm -COO^-$ groups. Notably, the appearance of C-COOstretching at 913 cm⁻¹ and COObending at 1,420 cm⁻¹ in the Raman spectrum of PAAZn nanospheres further indicated the complexation of $\rm Zn^{2+}$ with PAA [44,45]. Fig. S9 shows the FTIR curves of pure PAA and PAAZn nanospheres. Similarly, the interaction between $\rm Zn^{2+}$ and $\rm -COO^-$ in the PAAZn nanospheres induced significant changes and shifts to the peaks that correspond to $\rm -OH$ vibration at 1,451 cm⁻¹ and $\rm -COOH$ vibration at 1,701 cm⁻¹ in pure PAA [46,47], agreeing well with the phenomena observed in the Raman spectra shown in Fig. 1i.

Fig. 1j shows the XRD patterns of pure PAA and PAAZn nanospheres. Similar to pure PAA, the PAAZn nanospheres displayed a broad diffraction peak centered at 25°, which is a typical characteristic of amorphous polymers. The absence of diffraction peaks from Zn oxidation products, such as ZnO and Zn(OH)₂ [48], suggested the formation of a clean PAAZn complex. As shown in Fig. S10, the XRD curves of bare Zn and PAAZn@Zn further confirmed that no new crystalline phases were produced during etching. These characterization results provided strong evidences to support that the self-assembled nanospheres are the complexation product of Zn²⁺ and PAA.

To investigate the influence of the interfacial layer on the reversibility of Zn-metal anodes, morphologies of Zn deposits on bare Zn and PAAZn@Zn during cyclic plating/stripping were observed by SEM. After the first cycle, a large number of porous, mossy aggregates (Fig. 2a-b and Fig. S11) of Zn deposits were randomly distributed on the surface of bare Zn, suggesting the uneven plating/stripping behavior of the bare Zn anode due to its irregular surface morphology and the poor wetting between Zn and electrolyte [49-51]. As shown in Fig. S12a-c and Fig. 2cd, the surface of the bare Zn anode remained uneven in the subsequent cycles. The height of a typical Zn aggregate reached approximately 32 (Fig. S12c) and 34 μm (Fig. 2d) after 10 and 30 cycles, respectively. The fast Zn dendrite growth could be attributed to the high electric field intensity around the protuberances on the surface of bare Zn, thus attracting excessive Zn²⁺ around the tip and promoting highly localized Zn depositions [52,53]. Notably, a large amount of residual glass fibers from the separators were embedded in Zn deposits (Fig. 2a-d) because of the progressive, vertical growth of Zn dendrites, which can eventually trigger the internal short circuit in batteries. In contrast, Zn deposits were uniformly distributed in the nanoconfined spaces between PAAZn nanospheres on the surface of PAAZn@Zn (Fig. 2e-f) at the initial state, which effectively prevented the formation of large dendrites and porous, mossy aggregates. As shown in Fig. S12d-f, the evenly distributed Zn deposits with a thickness of approximately 5 µm co-existed with numerous PAAZn nanospheres after 10 cycles. After 30 cycles, the PAAZn@Zn anode retained an even and flat surface, and the thickness of the Zn deposits increased to around 8 µm (Fig. 2 g-h and Fig. S13). In addition, the continuous PAAZn interlayer turned into scattered nanospheres mixed with Zn deposits. During cycling, the chemical structure of the PAAZn nanospheres remained stable, as indicated by the characteristic peaks of PAAZn in the Raman (Fig. S14) and FTIR (Fig. S15) spectra of cycled PAAZn@Zn anodes. These results suggested that the nanoporous PAAZn interlayer could significantly regulate dendrite growth by facilitating uniform Zn deposition at the Zn/electrolyte interface, thus enabling highly reversible Zn metal anodes during longterm cycling.

The anti-corrosive behavior of PAAZn@Zn was investigated by Tafel and linear sweep voltammetry (LSV) tests in a three-electrode configuration. Fig. 2i shows the comparative Tafel curves of bare Zn and PAAZn@Zn electrodes in 2 M ZnSO₄ electrolyte. Compared with bare Zn, a lower corrosion current density of 4.39 mA/cm² was achieved for the PAAZn@Zn electrode, suggesting that the nanoporous polyelectrolytic interlayer can effectively suppress the corrosion of Zn in the electrolyte. The superior anti-corrosive property of PAAZn@Zn was further confirmed by aging the electrode in 2 M ZnSO₄ electrolyte for 5 days. As shown in Fig. S16a-b, due to the fast corrosion of Zn metal in mild acidic electrolytes, large flakes and numerous vertically standing petals were observed on the surface of aged Zn. Comparatively, the

surface of PAAZn@Zn remained nearly intact (Fig. S16c-d), confirming that the interfacial PAAZn layer can act as a physical barrier to protect Zn metal from corrosions and undesirable side reactions in aqueous electrolytes.

Additionally, the hydrogen evolution behaviors (Fig. 2j) of bare Zn and PAAZn@Zn were investigated by LSV tests in 1 M Na2SO4 electrolyte. The PAAZn@Zn electrode exhibited a significantly lower current density (-5 mA/cm²) of HER than that (-12.5 mA/cm²) of bare Zn electrode at -2.0 V vs Ag/AgCl. Moreover, the HER onset potential (-1.89 V vs Ag/AgCl) of the PAAZn@Zn electrode was noticeable higher than that (-1.85 V vs Ag/AgCl) of bare Zn electrode. These results demonstrated that the nanoporous yet densely packed PAAZn nanospheres can synergistically regulate dendrite growth and suppress hydrogen evolution at the Zn/electrolyte interface because of their unique chemical compositions and nanostructures, as schematically illustrated in Fig. 2k-l. In the aqueous electrolytes, bare Zn underwent heterogeneous nucleation and sequential rapid dendrite growth (Fig. 2k) during cyclic plating/stripping due to its irregular geometries [54]. Meanwhile, the competitive HER – reduction of H₂O to H₂ (Fig. 2k) proceeded continuously throughout the entire electrochemical process, and the HER could become worse in the presence of Zn dendrites and porous Zn deposits [52]. As illustrated in Fig. 2l, both dendrite growth and HER can be substantially suppressed because of the existence of the nanoporous PAAZn interlayer, which not only acted as a physical barrier to alleviate Zn metal from corrosions in aqueous electrolytes but also facilitate homogeneous deposition of Zn.

To further investigate the Zn nucleation and deposition mechanisms, chronoamperometry (CA) tests were conducted with an overpotential of -150 mV (Fig. 3a). For bare Zn electrode, the current density rapidly increased to 25.5 mA/cm² within 150 s, suggesting the long 2D diffusion process and remarkable tipping effect induced by dendrite growth. Zn ions can be preferentially absorbed on the tips of Zn dendrites and then deposited locally to promote the vertical growth of Zn dendrites [55]. In comparison, PAAZn@Zn electrode displayed a stable 3D diffusion behavior with a low current density of 12.1 mA/cm² after the initial Zn nucleation and 2D diffusion processes, implying that the nanoporous PAAZn interlayer could facilitate uniform Zn nucleation and deposition [56]. Fig. 3b displays the nucleation overpotential (NOP) obtained in Cu||Zn half cells at a current density of 1 mA/cm². The PAAZn@Zn anode exhibited a NOP of 30.0 mV, lower than that (38.2 mV) of bare Zn anode. This suggested that the nanoporous PAAZn interlayer effectively reduced the energy barrier for Zn nucleation [57]. Moreover, as shown in Fig. 3c, the Cul|PAAZn@Zn half cell possessed a high average Coulombic efficiency (CE) of 99.54 % over 150 cycles due to alleviated side reactions between water and Zn [58,59].

To understand the advantages of the nanoporous PAAZn interlayer, Raman tests were conducted to investigate the influence of PAAZn nanospheres on the chemical structure of water at the PAAZn@Zn/ electrolyte interface, as shown in Fig. S17. The baseline electrolyte (BE, 2 M ZnSO₄ in water) showed a typical broad peak associated with O-H stretching vibration ranging from 2,900 to 3,600 $\mathrm{cm}^{-1}\ \mathrm{due}$ to the presence of water [60]. In comparison, the O-H stretching vibration peak showed a lower intensity and was blue-shifted by PAAZn nanospheres, suggesting limited free water molecules and suppressed water activities at the PAAZn@Zn/electrolyte interface [61]. Furthermore, molecular dynamics (MD) simulations were performed to investigate the interactions between PAAZn and water (Fig. S18, see details in SI). Fig. S19 shows the radial distribution function – g(r) of the Zn^{2+} from ZnSO₄ or PAAZn with respect to the oxygen atom in water molecules. The results showed that the first peak of the g(r) of Zn²⁺ from ZnSO₄ was located at 2.07 Å, in good agreement with previous findings [62]. However, due to the strong interaction between PAAZn and water molecules, the first peak of the g(r) of electrostatically bonded Zn^{2+} in PAAZn molecule shifted to 1.80 Å. Moreover, the lower peak intensity of the g(r) implied that the Zn ions in PAAZn were less solvated by water molecules compared to those in the bulk electrolyte, which could

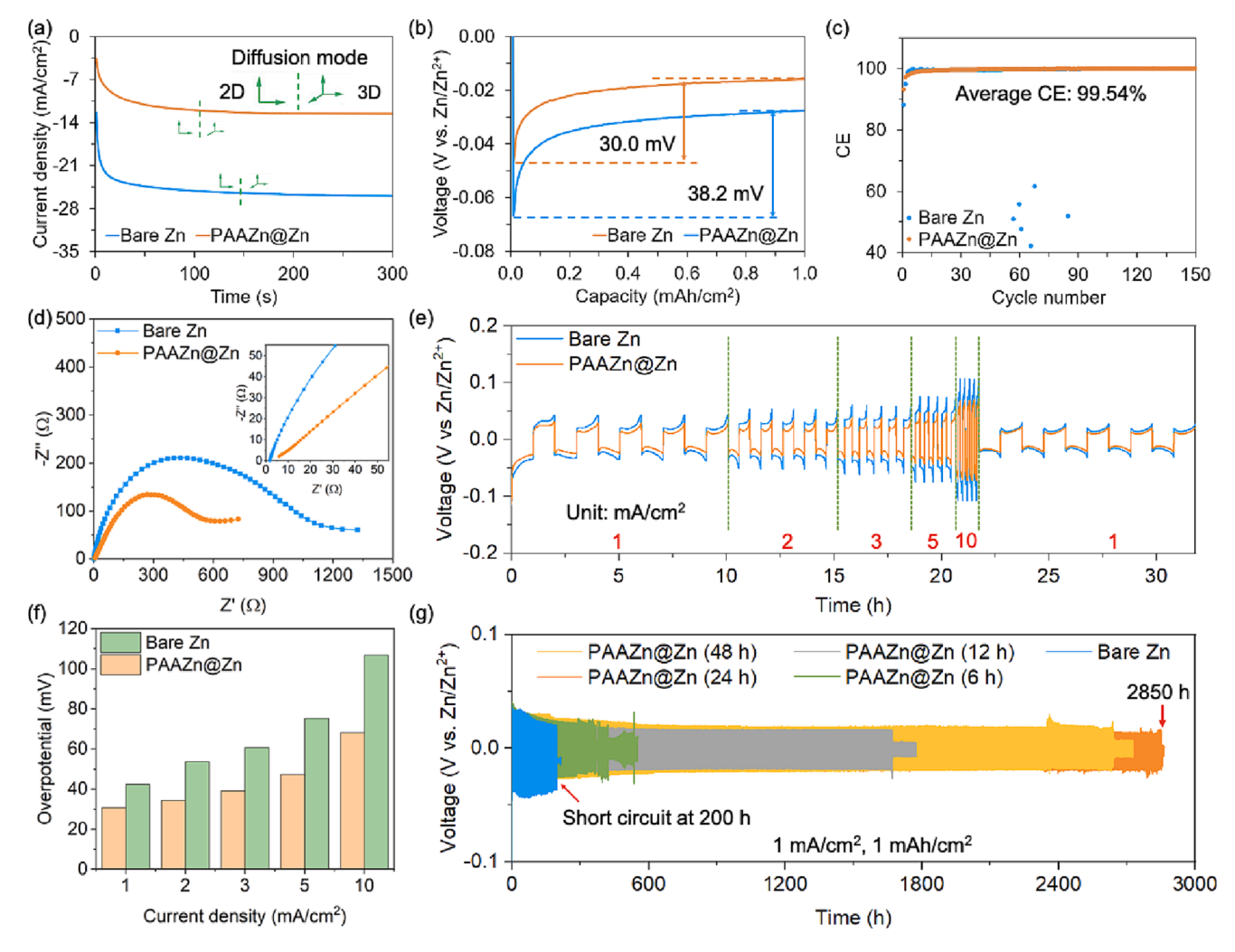


Fig. 3. Electrochemical performance of symmetric cells based on bare Zn and PAAZn@Zn electrodes. (a) CA curves of bare Zn and PAAZn@Zn electrodes. (b) Voltage curves and (c) CEs of Cu||Zn half cells based on bare Zn and PAAZn@Zn electrodes. (d) Comparative EIS curves of bare Zn- and PAAZn@Zn-based symmetric cells. (e) Rate capabilities of Zn||Zn and PAAZn@Zn||PAAZn@Zn symmetric cells at different current densities ranging from 1 to 10 mA/cm². (f) The initial voltage hysteresis of Zn||Zn and PAAZn@Zn||PAAZn@Zn symmetric cells at different current densities derived from the rate test. (g) Long-term voltage—time profiles of Zn||Zn and PAAZn@Zn||PAAZn@Zn symmetric cells at a plating/stripping current density of 1 mA/cm² and a capacity of 1 mAh/cm².

enhance the kinetics and reversibility of Zn plating/stripping at the PAAZn@Zn/electrolyte interface [63].

To investigate the effectiveness of the nanoporous protective layer at the cell level, electrochemical tests were conducted on Zn||Zn and PAAZn@Zn||PAAZn@Zn symmetric cells. Fig. 3d shows the comparative electrochemical impedance spectroscopy (EIS) curves of bare Zn-and PAAZn@Zn-based symmetric cells. Both EIS curves displayed a typical semicircle, which can be used to determine charge transfer resistance (Rct). Compared with the typical Zn||Zn symmetric cell, the PAAZn@Zn-based cell possessed a significantly lower Rct (~500 Ω) and a slightly higher interfacial resistance (Rs, 6.0 Ω). The low Rct of PAAZn@Zn suggested that the nanoporous PAAZn greatly facilitated the charge transfer kinetics at the Zn/electrolyte interface, which could be attributed to the excellent electrolyte–electrode wetting [64] and the abundant carboxyl groups in PAAZn molecules that could effectively reconstruct the solvation structure of Zn ions [5].

Fig. 3e-f shows the rate capabilities and voltage hysteresis of the bare Zn- and PAAZn@Zn-based symmetric cells. The voltage hysteresis of the Zn||Zn cell increased from 42.4 to 104.9 mV when increasing current density from 1 to 10 mA/cm². Comparatively, the PAAZn@Zn-based symmetric cell exhibited stable and low voltage hysteresis of 30.7, 34.4, 39.1, 47.3, and 68.2 mV in the range of 1–10 mA/cm², much lower than those of the Zn||Zn symmetric cell (Fig. 3f) and other symmetric

cells reported in previous studies (Table S1). Moreover, the voltage hysteresis (21.0 mV) of the PAAZn@Zn-based symmetric cell remained stable and was lower than that (28.9 mV) of the Zn||Zn symmetric cell when switching the current density from 10 to 1 mA/cm². These results implied that PAAZn@Zn electrodes required lower voltage activation during cyclic plating/stripping because of their fast charge transfer kinetics [51], agreeing well with the EIS results presented in Fig. 3d.

Further, long-term galvanostatic cycling tests of Zn||Zn and PAAZn@Zn||PAAZn@Zn symmetric cells were performed at a current density of 1 mA/cm² with the plating/stripping capacity of 1 mAh/cm² (Fig. 3g). Such a plating/stripping condition has been widely used to evaluate the reversibility of Zn metal anodes [33,56,61,65]. After 200 h of plating/stripping, the overpotential of Zn||Zn suddenly dropped to approximately zero, suggesting the internal short circuit in the symmetric cell triggered by rapid dendrite growth and severe hydrogen evolution. In the presence of a nanoporous PAAZn interlayer, the cycle life of symmetric cells could be significantly enhanced. Notably, when the Zn metal was etched with an optimal time of 24 h, the PAAZn@Znbased symmetric cell showed a significantly extended lifespan of 2,850 h, surpassing those of symmetric cells reported in previous studies (Table S1). During the entire cycling process, the PAAZn@Zn-based symmetric cell exhibited low plating/stripping voltages, indicating its fast charge transfer kinetics. Even at high current densities up to 5 mA/

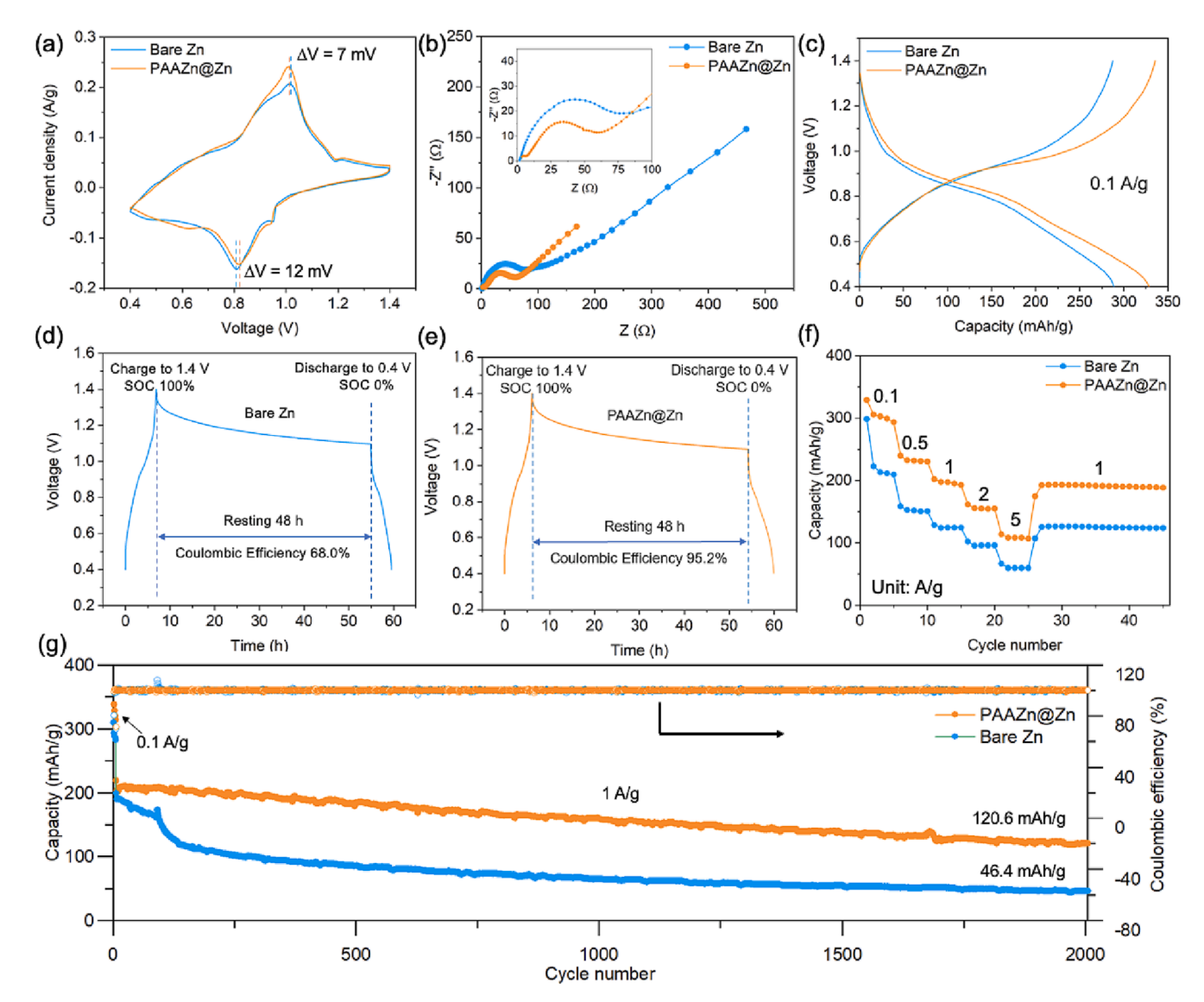


Fig. 4. Electrochemical performance of full cells based on bare Zn and PAAZn@Zn anodes. (a) CV curves of Zn||NVO and PAAZn@Zn||NVO full cells at a scan rate of 0.1 mV/s. (b) EIS curves of Zn||NVO and PAAZn@Zn||NVO full cells in the frequency ranging from 0.01 Hz to 100 kHz. (c) Charge/discharge curves of Zn||NVO and PAAZn@Zn||NVO full cells at a current density of 0.1 A/g. (d) and (e) Self-discharge tests of Zn||NVO and PAAZn@Zn||NVO full cells. (f) Rate tests of Zn||NVO and PAAZn@Zn||NVO full cells. (g) Long-term cyclic tests of Zn||NVO and PAAZn@Zn||NVO full cells at a current density of 1 A/g.

cm², the PAAZn@Zn-based symmetric cells still exhibited excellent stability over 2,000 cycles (Fig. S20). The long lifespan and high stability of PAAZn@Zn-based symmetric cells confirmed that the nanoporous PAAZn layer could effectively suppress the dendrite growth and HER, thus ensuring the extraordinary reversibility of Zn metal anodes and the superior long-term cycling stability of PAAZn@Zn-based symmetric cells in aqueous electrolytes.

Fig. 4 shows the electrochemical performance of bare Zn- and PAAZn@Zn-based full cells paired with sodium-doped V_2O_5 (NVO) cathodes in 2 M ZnSO₄. The NVO nanoneedles were prepared following the procedures described in prior work [66], and their structures were verified by SEM (Fig. S21) and XRD (Fig. S22). The SEM image and XRD of NVO-coated carbon paper as cathodes were further presented in Fig. S23 and Fig. S24, respectively. Fig. 4a-b shows the comparative cyclic voltammetry (CV) and EIS curves of the two typical Zn||NVO and PAAZn@Zn||NVO full cells. The PAAZn@Zn||NVO full cell possessed lower voltage polarizations (Fig. 4a) and a smaller R_{ct} (Fig. 4b) compared with Zn||NVO, suggesting the fast charge transfer kinetics in the presence of PAAZn nanospheres and agreeing well with the results obtained in the symmetric cells. Meanwhile, as indicated by the similar

redox peaks of the CV curves of both cells, PAAZn nanospheres were electrochemically inert and exerted no influence on the electrochemical reactions during charge/discharge. The charge/discharge curves (Fig. 4c) of Zn||NVO and PAAZn@Zn||NVO full cells further confirmed that they have similar Zn $^{2+}$ insertion/extraction behavior, coinciding well with the results obtained from CV tests (Fig. 4a). The influence of the nanoporous PAAZn layer on parasitic reactions was further evaluated by self-discharge tests (Fig. 4d-e). The results showed that the Zn|| NVO cell exhibited a relatively low CE of 68.0 % after resting for 48 h, while the CE of the PAAZn@Zn||NVO cell significantly increased to 95.2 % under the same conditions. This phenomenon strongly suggested that the interfacial layer of nanoporous PAAZn can effectively suppress parasitic reactions such as Zn corrosion and H $_2$ evolution.

Fig. 4f shows the rate capabilities of full cells at various current densities ranging from 0.1 to 5 A/g. The corresponding charge/discharge curves of the PAAZn@Zn||NVO full cell are given in Fig. S25. The Zn||NVO full cell displayed inferior rate capabilities and low capacities (e.g., 128.6 mAh/g at 1 A/g), which could be attributed to the sluggish charge transfer kinetics and severe side reactions occurring at Zn/electrolyte interfaces [67]. On the contrary, the PAAZn@Zn||NVO

full cell delivered higher discharge capacities of 329.1, 239.9, 202.2, 161.7, and 113.9 mAh/g with increasing current densities of 0.1, 0.5, 1, 2, and 5 A/g, respectively. The superior rate capabilities of the PAAZn@Zn||NVO full cell suggested that the nanoporous PAAZn interlayer facilitated fast ion transport through the artificial interface. When the current density switched from 5 to 1 A/g, the PAAZn@Zn|| NVO cell displayed a stable discharge capacity of 192.5 mAh/g, corresponding to a capacity retention rate of 95.2 % compared to that (202.2 mAh/g) of the first cycle at 1 A/g. As shown in Fig. S26, in sharp contrast to the surface of bare Zn with large amounts of vertically standing and porous Zn deposits, the surface of PAAZn@Zn after the rate tests retained its original structure and exhibited a dendrite-free morphology. Fig. 4g further demonstrates the comparative long-term cyclic stability of Zn||NVO and PAAZn@Zn||NVO full cells at a current density of 1 A/g. The PAAZn@Zn||NVO full cell delivered an initial discharge capacity of 204.2 mAh/g and remained 120.6 mAh/g after 2,000 charge/discharge cycles with a stable CE of nearly 100 %, while the discharge capacities of Zn||NVO full cell decreased substantially from 190.8 to 46.4 mAh/g. As shown in Fig. S27, at a low current density of 0.1 A/g, the PAAZn@Zn|| NVO full cell exhibited a capacity retention rate of 77.4 % after 100 cycles, higher than that (35.7 %) of the Zn||NVO full cell. These results confirmed that the nanoporous PAAZn interlayer could effectively improve the reversibility of Zn metal anodes for high-performance AZIBs.

3. Conclusions

In this work, we designed a highly stable Zn metal anode chemically modified with a self-assembled, nanoporous PAAZn interlayer via a facile solution-based process. Because of its unique nanostructures and chemical compositions, the nanoporous PAAZn interlayer between Zn and electrolyte not only effectively regulated the dendrite growth but also significantly suppressed the hydrogen evolutions. In comparison to bare Zn, the voltage polarizations of Zn plating/stripping were largely decreased with the modification of PAAZn. Consequently, highly reversible Zn plating/stripping was achieved even at high current densities. Moreover, a significantly prolonged cycle life up to 2,850 h was achieved for PAAZn@Zn-based symmetric cells while bare Zn-based symmetric cells failed after 200 h. Compared with Zn||NVO full cells (e.g., 46.4 mAh/g), PAAZn@Zn||NVO full cells can deliver a substantially higher capacity of 120.6 mAh/g at a current density of 1 A/g after 2,000 charge/discharge cycles. These results highlight the importance of synergistically regulating the dendrite growth and suppressing the hydrogen evolution reaction for highly reversible Zn metal anodes. The findings of our work contribute to an in-depth understanding of the functionalities of nanoporous polyelectrolytic interlayers and provide a new strategy for the design of high-performance Zn metal anodes.

4. Experimental procedures

4.1. Material synthesis

Bare Zn discs (100 $\mu m,~\Phi 14$ mm) were cleaned with 0.05 M $H_2SO_4,$ isopropyl alcohol, and ultra-pure (18 $M\Omega)$ water sequentially. The PAAZn@Zn electrode was prepared by etching the cleaned Zn discs in PAA solutions (2 g/L, average $M_w \sim 450,000)$ for 6, 12, and 24 h. After that, the obtained PAAZn@Zn anodes were thoroughly washed with ultra-pure water to remove PAA residues and were dried under ambient conditions for further tests. The PAAZn nanospheres can uniformly cover the entire surface of Zn foil after 24 h, which was considered the optimal etching time. Therefore, the as-obtained PAAZn@Zn electrodes after etching for 24 h were selected for electrochemical tests unless otherwise noted.

4.2. Material characterization

Scanning electron microscopy (SEM) and energy dispersive X-ray analysis (EDAX) were conducted on a field emission scanning electron microscope (Supra 40, Zeiss). The material structures were analyzed by X-ray photoelectron spectroscopy (XPS, Versa Probe II), Raman spectroscopy (NRS-5100, Jasco), Fourier transformation infrared spectroscope (FTIR, Agilent 660) and X-ray diffraction (XRD, Rigaku Ultima IV diffractometer). Contact angles of bare Zn and PAAZn@Zn were measured by a goniometer (Kruss DSA 100) with a droplet size of 10 µL.

4.3. Cell assembling

The Zn||Zn symmetric cells were assembled using Zn discs with a thickness of 0.1 mm and diameter of 14 mm. The glass fiber (Φ16 mm, GF/D, Whatman) and 2 M ZnSO₄ (100 µL) were used as separator and electrolyte, respectively. The cathode material - sodium-doped vanadium oxide (NVO) was prepared by the hydrothermal method reported in prior work [66]. Briefly, 3.638 g V₂O₅ and 0.8 g NaOH were added into 80 mL of ultra-pure water under magnetically stirring for 4 h. After that, the solution was transferred to a 200 mL autoclave and kept at 180 °C for 48 h. The solid products after hydrothermal treatment were collected and centrifuged with ultra-pure water at 5,000 RPM for 15 min and repeated 5 times. The sediments after centrifuge were freeze-dried for 48 h followed by vacuum drying at 80 °C for 12 h to obtain the final active materials. The active material (NVO), carbon black, and binder (PVDF) were mixed in a weight ratio of 7:2:1 and grinded with NMP to form a slurry. Then, the slurry was uniformly coated on carbon paper ($10 \times 10 \text{ cm}^2$) and dried under vacuum at 80 °C overnight. The mass loading of the active materials was $1.5 \sim 2 \text{ mg/cm}^2$. Finally, the NVO electrodes were obtained by punching the NVO-coated carbon paper into Φ 14 mm discs and were used as the cathode for assembling full cells.

4.4. Electrochemical measurements

All the cells were rested for 2 h before electrochemical tests. The cyclic voltammetry (CV, 0.4 – 1.4 V), linear sweep voltammetry (LSV), Tafel, and electrochemical impedance spectroscopy (EIS, 0.01 Hz–100 kHz) tests were conducted on an electrochemical workstation (Interface 1010E, Gamry). Among them, Tafel and LSV tests of bare Zn and PAAZn@Zn electrodes were performed in a three-electrode configuration, in which Zn or PAAZn@Zn plate (1 \times 2 cm²), Pt mesh, and Ag/AgCl electrode were used as the working, counter, and reference electrodes, respectively. Tafel tests were performed in 2 M ZnSO4 electrolyte with voltage window between -300 to 300 mV vs the open circuit potential at a scan rate of 1 mV/s. LSV measurements were carried out in 1 M Na2SO4 at a sweep rate of 5 mV/s from -1.1 V to -2.0 V. Galvanostatic charge—discharge and chronopotentiometry tests were performed on a multi-channel battery testing system (NEWARE). All the electrochemical tests were performed under ambient conditions.

Declaration of Competing Interest

The authors declare that they have no known competing financial interests or personal relationships that could have appeared to influence the work reported in this paper.

Data availability

Data will be made available on request.

Acknowledgments

G.X. thanks the University of Texas at Dallas startup fund and the support from the NSF (Grant No. CBET-1949962). T.L. thanks the

support from the NSF (Grant No. CBET-1949910) for support. The authors thank Prof. S. M. You for the help with the contact angle measurements.

Appendix A. Supplementary data

Supplementary data to this article can be found online at https://doi.org/10.1016/j.cej.2023.142276.

References

- D. Chao, W. Zhou, F. Xie, C. Ye, H. Li, M. Jaroniec, S.-Z. Qiao, Roadmap for advanced aqueous batteries: From design of materials to applications, Sci. Adv. 6 (21) (2020)
- [2] J.O.G. Posada, A.J.R. Rennie, S.P. Villar, V.L. Martins, J. Marinaccio, A. Barnes, C. F. Glover, D.A. Worsley, P.J. Hall, Aqueous batteries as grid scale energy storage solutions, Renew. Sustain. Energy Rev. 68 (2017) 1174–1182.
- [3] H. Wang, R. Tan, Z. Yang, Y. Feng, X. Duan, J. Ma, Stabilization perspective on metal anodes for aqueous batteries, Adv. Energy Mater. 11 (2) (2021) 2000962.
- [4] F. Wang, O. Borodin, T. Gao, X. Fan, W. Sun, F. Han, A. Faraone, J.A. Dura, K. Xu, C. Wang, Highly reversible zinc metal anode for aqueous batteries, Nat. Mater. 17 (6) (2018) 543–549.
- [5] R. Chen, Q. Liu, L. Xu, X. Zuo, F. Liu, J. Zhang, X. Zhou, L. Mai, Zwitterionic bifunctional layer for reversible Zn anode, ACS Energy Lett. 7 (5) (2022) 1719–1727.
- [6] W. Yang, Y. Yang, H. Yang, H. Zhou, Regulating water activity for rechargeable zinc-ion batteries: progress and perspective, ACS Energy Lett. 7 (8) (2022) 2515–2530.
- [7] H. Fu, L. Xiong, W. Han, M. Wang, Y.J. Kim, X. Li, W. Yang, G. Liu, Highly active crystal planes-oriented texture for reversible high-performance Zn metal batteries, Energy Storage Mater. 51 (2022) 550–558.
- [8] W. Du, J. Yan, C. Cao, C.C. Li, Electrocrystallization orientation regulation of zinc metal anodes: strategies and challenges, Energy Storage Mater. 52 (2022) 329–354.
- [9] J. Zhou, M. Xie, F. Wu, Y. Mei, Y. Hao, R. Huang, G. Wei, A. Liu, L. Li, R. Chen, Ultrathin surface coating of nitrogen-doped graphene enables stable zinc anodes for aqueous zinc-ion batteries, Adv. Mater. 33 (33) (2021) 2101649.
- [10] S. Guo, L. Qin, T. Zhang, M. Zhou, J. Zhou, G. Fang, S. Liang, Fundamentals and perspectives of electrolyte additives for aqueous zinc-ion batteries, Energy Storage Mater. 34 (2021) 545–562.
- [11] Y. Geng, L. Pan, Z. Peng, Z. Sun, H. Lin, C. Mao, L. Wang, L. Dai, H. Liu, K. Pan, X. Wu, Q. Zhang, Z. He, Electrolyte additive engineering for aqueous Zn ion batteries, Energy Storage Mater. 51 (2022) 733–755.
- [12] T.-T. Su, K. Wang, B.-Y. Chi, W.-F. Ren, R.-C. Sun, Stripy zinc array with preferential crystal plane for the ultra-long lifespan of zinc metal anodes for zinc ion batteries, EcoMat 4 (6) (2022) e12219.
- [13] M. Zhou, S. Guo, J. Li, X. Luo, Z. Liu, T. Zhang, X. Cao, M. Long, B. Lu, A. Pan, G. Fang, J. Zhou, S. Liang, Surface-preferred crystal plane for a stable and reversible zinc anode, Adv. Mater. 33 (21) (2021) 2100187.
- [14] Z. Huang, H. Li, Z. Yang, H. Wang, J. Ding, L. Xu, Y. Tian, D. Mitlin, J. Ding, W. Hu, Nanosecond laser lithography enables concave-convex zinc metal battery anodes with ultrahigh areal capacity, Energy Storage Mater. 51 (2022) 273–285.
- [15] Y. Song, P. Ruan, C. Mao, Y. Chang, L. Wang, L. Dai, P. Zhou, B. Lu, J. Zhou, Z. He, Metal-organic frameworks functionalized separators for robust aqueous zinc-ion batteries, Nano-Micro Lett. 14 (1) (2022) 218.
- [16] C. Liu, Z. Luo, W. Deng, W. Wei, L. Chen, A. Pan, J. Ma, C. Wang, L. Zhu, L. Xie, X.-Y. Cao, J. Hu, G. Zou, H. Hou, X. Ji, Liquid alloy interlayer for aqueous Zinc-ion battery, ACS Energy Lett. 6 (2) (2021) 675–683.
- [17] Q. Lu, C. Liu, Y. Du, X. Wang, L. Ding, A. Omar, D. Mikhailova, Uniform Zn deposition achieved by Ag coating for improved aqueous zinc-ion batteries, ACS Appl. Mater. Interfaces 13 (14) (2021) 16869–16875.
- [18] C. Liu, Q. Lu, A. Omar, D. Mikhailova, A facile chemical method enabling uniform Zn deposition for improved aqueous Zn-ion batteries, Nanomaterials 11 (3) (2021) 764
- [19] M. Cui, Y. Xiao, L. Kang, W. Du, Y. Gao, X. Sun, Y. Zhou, X. Li, H. Li, F. Jiang, C. Zhi, Quasi-isolated Au particles as heterogeneous seeds to guide uniform Zn deposition for aqueous zinc-ion batteries, ACS Appl. Energy Mater. 2 (9) (2019) 6490–6496.
- [20] C. Mao, Y. Chang, X. Zhao, X. Dong, Y. Geng, N. Zhang, L. Dai, X. Wu, L. Wang, Z. He, Functional carbon materials for high-performance Zn metal anodes, J. Energy Chem. 75 (2022) 135–153.
- [21] H. Qin, W. Kuang, D. Huang, X. Zhang, J. Liu, L. Yi, F. Shen, Z. Wei, Y. Huang, J. Xu, H. He, Achieving high-rate and high-capacity Zn metal anodes via a three-inone carbon protective layer, J. Mater. Chem. A 10 (34) (2022) 17440–17451.
- [22] J. Shin, J. Lee, Y. Kim, Y. Park, M. Kim, J.W. Choi, Highly reversible, grain-directed zinc deposition in aqueous zinc ion batteries, Adv. Energy Mater. 11 (39) (2021) 2100676.
- [23] Y. Jiao, F. Li, X. Jin, Q. Lei, L. Li, L. Wang, T. Ye, E. He, J. Wang, H. Chen, J. Lu, R. Gao, Q. Li, C. Jiang, J. Li, G. He, M. Liao, H. Zhang, I.P. Parkin, H. Peng, Y. Zhang, Engineering polymer glue towards 90% zinc utilization for 1000 hours to make high-performance Zn-ion batteries, Adv. Funct. Mater. 31 (49) (2021) 2107652.

- [24] Z. Cao, X. Zhu, D. Xu, P. Dong, M.O.L. Chee, X. Li, K. Zhu, M. Ye, J. Shen, Eliminating Zn dendrites by commercial cyanoacrylate adhesive for zinc ion battery, Energy Storage Mater. 36 (2021) 132–138.
- [25] H. He, H. Tong, X. Song, X. Song, J. Liu, Highly stable Zn metal anodes enabled by atomic layer deposited Al₂O₃ coating for aqueous zinc-ion batteries, J. Mater. Chem. A 8 (16) (2020) 7836–7846.
- [26] Z. Guo, L. Fan, C. Zhao, A. Chen, N. Liu, Y. Zhang, N. Zhang, A dynamic and self-adapting interface coating for stable Zn-metal anodes, Adv. Mater. 34 (2) (2022) 2105133.
- [27] X. Zhou, P. Cao, A. Wei, A. Zou, H. Ye, W. Liu, J. Tang, J. Yang, Driving the interfacial ion-transfer kinetics by mesoporous TiO₂ spheres for high-performance aqueous Zn-ion batteries, ACS Appl. Mater. Interfaces 13 (7) (2021) 8181–8190.
- [28] B. Li, J. Xue, X. Lv, R. Zhang, K. Ma, X. Wu, L. Dai, L. Wang, Z. He, A facile coating strategy for high stability aqueous zinc ion batteries: Porous rutile nano-TiO₂ coating on zinc anode, Surf. Coat. Technol. 421 (2021), 127367.
- [29] L. Kang, M. Cui, F. Jiang, Y. Gao, H. Luo, J. Liu, W. Liang, C. Zhi, Nanoporous CaCO₃ coatings enabled uniform Zn stripping/plating for long-life zinc rechargeable aqueous batteries, Adv. Energy Mater. 8 (25) (2018) 1801090.
- [30] X. Han, H. Leng, Y. Qi, P. Yang, J. Qiu, B. Zheng, J. Wu, S. Li, F. Huo, Hydrophilic silica spheres layer as ions shunt for enhanced Zn metal anode, Chem. Eng. J. 431 (2022), 133931.
- [31] P. Liang, J. Yi, X. Liu, K. Wu, Z. Wang, J. Cui, Y. Liu, Y. Wang, Y. Xia, J. Zhang, Highly reversible Zn anode enabled by controllable formation of nucleation sites for Zn-based batteries, Adv. Funct. Mater. 30 (13) (2020) 1908528.
- [32] Y. Liu, T. Guo, Q. Liu, F. Xiong, M. Huang, Y. An, J. Wang, Q. An, C. Liu, L. Mai, Ultrathin ZrO₂ coating layer regulates Zn deposition and raises long-life performance of aqueous Zn batteries, Mater. Today Energy 28 (2022), 101056.
- [33] S. Zheng, L. Wei, Z. Zhang, J. Pan, J. He, L. Gao, C.C. Li, In situ polymerization of ionic liquid with tunable phase separation for highly reversible and ultralong cycle life Zn-ion battery, Nano Lett. 22 (22) (2022) 9062–9070.
- [34] Q. Liu, R. Chen, L. Xu, Y. Liu, Y. Dai, M. Huang, L. Mai, Steric molecular combing effect enables ultrafast self-healing electrolyte in quasi-solid-state zinc-ion batteries, ACS Energy Lett. 7 (8) (2022) 2825–2832.
- [35] T. Wang, C. Li, X. Xie, B. Lu, Z. He, S. Liang, J. Zhou, Anode materials for aqueous zinc ion batteries: Mechanisms, properties, and perspectives, ACS Nano 14 (12) (2020) 16321–16347.
- [36] I. Rianasari, F. Benyettou, S.K. Sharma, T. Blanton, S. Kirmizialtin, R. Jagannathan, A chemical template for synthesis of molecular sheets of calcium carbonate, Sci. Rep. 6 (1) (2016) 25393.
- [37] MR Shaik, M Kuniyil, M Khan, N Ahmad, A Al-Warthan, MRH Siddiqui, and SF Adil, Modified polyacrylic acid-zinc composites: Synthesis, characterization and biological activity. 2016. 21(3): p. 292.
- [38] N.-W. Li, Y. Shi, Y.-X. Yin, X.-X. Zeng, J.-Y. Li, C.-J. Li, L.-J. Wan, R. Wen, Y.-G. Guo, A flexible solid electrolyte interphase layer for long-life lithium metal anodes, Angew. Chem. Int. Ed. 57 (6) (2018) 1505–1509.
- [39] T. Swift, L. Swanson, M. Geoghegan, S. Rimmer, The pH-responsive behaviour of poly(acrylic acid) in aqueous solution is dependent on molar mass, Soft Matter 12 (9) (2016) 2542–2549.
- [40] M. Zhu, Q. Zhang, X. Xiao, B. Shi, A novel strategy for enhancing comprehensive properties of polyacrylate coating: Incorporation of highly dispersed zinc ions by using polyacrylic acid as carrier, Prog. Org. Coat. 162 (2022), 106596.
- [41] M. Todica, C.V. Pop, L. Udrescu, T. Stefan, Spectroscopy of a gamma irradiated poly(acrylic acid)-clotrimazole system, Chin. Phys. Lett. 28 (12) (2011) 128201.
- [42] M. Todica, R. Stefan, C.V. Pop, L. Olar, IR and Raman investigation of some poly (acrylic) acid gels in aqueous and neutralized state, Acta Phys. Pol. A 128 (1) (2015) 128–135.
- [43] J. Dong, Y. Ozaki, K. Nakashima, Infrared, Raman, and near-infrared spectroscopic evidence for the coexistence of various hydrogen-bond forms in poly(acrylic acid), Macromolecules 30 (4) (1997) 1111–1117.
- [44] S. Koda, H. Nomura, M. Nagasawa, Raman spectroscopic studies on the interaction between counterion and polyion, Biophys. Chem. 15 (1) (1982) 65–72.
- [45] A. Virya, K. Lian, Lithium polyacrylate-polyacrylamide blend as polymer electrolytes for solid-state electrochemical capacitors, Electrochem. Commun. 97 (2018) 77–81.
- [46] L.J. Kirwan, P.D. Fawell, W. van Bronswijk, In situ FTIR-ATR examination of poly (acrylic acid) adsorbed onto hematite at low pH, Langmuir 19 (14) (2003) 5802–5807.
- [47] J.A. Sánchez-Márquez, R. Fuentes-Ramírez, I. Cano-Rodríguez, Z. Gamiño-Arroyo, E. Rubio-Rosas, J.M. Kenny, N. Rescignano, Membrane made of cellulose acetate with polyacrylic acid reinforced with carbon nanotubes and its applicability for chromium removal, Int. J. Polym. Sci. 2015 (2015), 320631.
- [48] D. Weibel, Z.R. Jovanovic, E. Gálvez, A. Steinfeld, Mechanism of Zn particle oxidation by H₂O and CO₂ in the presence of ZnO, Chem. Mater. 26 (22) (2014) 6486–6495.
- [49] V. Yufit, F. Tariq, D.S. Eastwood, M. Biton, B. Wu, P.D. Lee, N.P. Brandon, Operando visualization and multi-scale tomography studies of dendrite formation and dissolution in zinc batteries, Joule 3 (2) (2019) 485–502.
- [50] G. Feng, J. Guo, H. Tian, Z. Li, Y. Shi, X. Li, X. Yang, D. Mayerich, Y. Yang, X. Shan, Probe the localized electrochemical environment effects and electrode reaction dynamics for metal batteries using in situ 3D microscopy, Adv. Energy Mater. 12 (3) (2022) 2103484.
- [51] Q. Li, A. Chen, D. Wang, Y. Zhao, X. Wang, X. Jin, B. Xiong, C. Zhi, Tailoring the metal electrode morphology via electrochemical protocol optimization for longlasting aqueous zinc batteries, Nat. Commun. 13 (1) (2022) 3699.

- [52] L. Hong, L.-Y. Wang, Y. Wang, X. Wu, W. Huang, Y. Zhou, K.-X. Wang, J.-S. Chen, Toward hydrogen-free and dendrite-free aqueous zinc batteries: Formation of zincophilic protective layer on Zn anodes, Adv. Sci. 9 (6) (2022) 2104866.
- [53] G. Xiong, P. He, Z. Lyu, T. Chen, B. Huang, L. Chen, T.S. Fisher, Bioinspired leaveson-branchlet hybrid carbon nanostructure for supercapacitors, Nat. Commun. 9 (1) (2018) 790.
- [54] J. Zhou, M. Peng, X. Xia, S. Qian, Z. Wang, C. Zhu, X. Zeng, H. Ji, S. Wang, X. Zhou, J. Liu, X. Shen, Y. Cheng, T. Qian, C. Yan, New type of dynamically "solid-liquid" interconvertible electrolyte for high-rate Zn metal battery, Nano Lett. 22 (7) (2022) 2898–2906.
- [55] F. Ding, W. Xu, G.L. Graff, J. Zhang, M.L. Sushko, X. Chen, Y. Shao, M. H. Engelhard, Z. Nie, J. Xiao, X. Liu, P.V. Sushko, J. Liu, J.-G. Zhang, Dendrite-free lithium deposition via self-healing electrostatic shield mechanism, J. Am. Chem. Soc. 135 (11) (2013) 4450–4456.
- [56] X. Nie, L. Miao, W. Yuan, G. Ma, S. Di, Y. Wang, S. Shen, N. Zhang, Cholinium cations enable highly compact and dendrite-free Zn metal anodes in aqueous electrolytes, Adv. Funct. Mater. 32 (32) (2022) 2203905.
- [57] Q. Zhang, J. Luan, L. Fu, S. Wu, Y. Tang, X. Ji, H. Wang, The three-dimensional dendrite-free zinc anode on a copper mesh with a zinc-oriented polyacrylamide electrolyte additive, Angew. Chem. Int. Ed. 58 (44) (2019) 15841–15847.
- [58] Y. Dong, L. Miao, G. Ma, S. Di, Y. Wang, L. Wang, J. Xu, N. Zhang, Non-concentrated aqueous electrolytes with organic solvent additives for stable zinc batteries, Chem. Sci. 12 (16) (2021) 5843–5852.

- [59] G. Ma, L. Miao, W. Yuan, K. Qiu, M. Liu, X. Nie, Y. Dong, N. Zhang, F. Cheng, Non-flammable, dilute, and hydrous organic electrolytes for reversible Zn batteries, Chem. Sci. 13 (38) (2022) 11320–11329.
- [60] D.M. Carey, G.M. Korenowski, Measurement of the Raman spectrum of liquid water, J. Chem. Phys. 108 (7) (1998) 2669–2675.
- [61] J. Zhu, Z. Bie, X. Cai, Z. Jiao, Z. Wang, J. Tao, W. Song, H.J. Fan, A molecular-sieve electrolyte membrane enables separator-free zinc batteries with ultralong cycle life, Adv. Mater. 34 (43) (2022) 2207209.
- [62] S. De, S.M. Ali, A. Ali, V.G. Gaikar, Micro-solvation of the Zn²⁺ ion—a case study, PCCP 11 (37) (2009) 8285–8294.
- [63] S. Liu, J. Mao, W.K. Pang, J. Vongsvivut, X. Zeng, L. Thomsen, Y. Wang, J. Liu, D. Li, Z. Guo, Tuning the electrolyte solvation structure to suppress cathode dissolution, water reactivity, and Zn dendrite growth in zinc-ion batteries, Adv. Funct. Mater. 31 (38) (2021) 2104281.
- [64] Q. Li, A. Chen, D. Wang, Z. Pei, C. Zhi, "Soft shorts" hidden in zinc metal anode research, Joule 6 (2) (2022) 273–279.
- [65] P. Xiao, H. Li, J. Fu, C. Zeng, Y. Zhao, T. Zhai, H. Li, An anticorrosive zinc metal anode with ultra-long cycle life over one year, Energ. Environ. Sci. 15 (4) (2022) 1638–1646.
- [66] J. Zhou, L. Zhang, M. Peng, X. Zhou, Y. Cao, J. Liu, X. Shen, C. Yan, T. Qian, Diminishing interfacial turbulence by colloid-polymer electrolyte to stabilize zinc ion flux for deep-cycling Zn metal batteries, Adv. Mater. 34 (21) (2022) 2200131.
- [67] H. Zhang, S. Li, L. Xu, R. Momen, W. Deng, J. Hu, G. Zou, H. Hou, X. Ji, High-yield carbon dots interlayer for ultra-stable zinc batteries, Adv. Energy Mater. 12 (26) (2022) 2200665.